

OPEN ACCESS

# Mn-Based Transition Metal Oxide Positive Electrode for K-Ion Battery Using an FSA-based Ionic Liquid Electrolyte

To cite this article: Kai Jiao *et al* 2024 *J. Electrochem. Soc.* **171** 100510

View the [article online](#) for updates and enhancements.

## You may also like

- [Developing Robust Potassium-Ion Batteries Using Sodium Insertion Host Materials](#)  
Sada Krishnakanth, Senthilkumar Baskar and Prabeer Barpanda
- [Emerging ferroelectric transistors with nanoscale channel materials: the possibilities, the limitations](#)  
Xia Hong
- [MnO<sub>2</sub>@In<sub>2</sub>O<sub>3</sub> Nanotubes as Cathode Material for Aqueous Rechargeable Zn-Ion Battery with High Electrochemical Performance](#)  
Lei Gou, Dong Xue, Ke-Liang Mou et al.

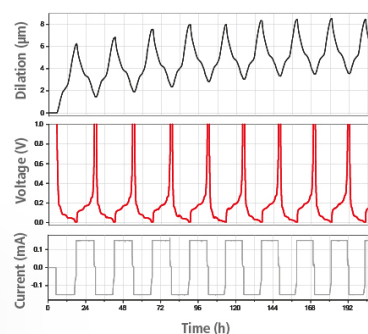
## Watch Your Electrodes Breathe!

Measure the Electrode Expansion in the Nanometer Range with the ECD-4-nano.

- ✓ Battery Test Cell for Dilatometric Analysis (Expansion of Electrodes)
- ✓ Capacitive Displacement Sensor (Range 250  $\mu\text{m}$ , Resolution  $\leq 5$  nm)
- ✓ Detect Thickness Changes of the Individual Half Cell or the Full Cell
- ✓ Additional Gas Pressure (0 to 3 bar) and Temperature Sensor (-20 to 80° C)



**EL-CELL**<sup>®</sup>  
electrochemical test equipment



See Sample Test Results:



Scan me!

Download the Data Sheet (PDF):



Scan me!

Or contact us directly:

+49 40 79012-734

sales@el-cell.com

www.el-cell.com



# Mn-Based Transition Metal Oxide Positive Electrode for K-Ion Battery Using an FSA-based Ionic Liquid Electrolyte

Kai Jiao,<sup>1</sup> Takayuki Yamamoto,<sup>1,\*</sup> Hisao Kiuchi,<sup>2</sup> Haochong Zhao,<sup>2</sup> and Toshiyuki Nohira<sup>1,\*</sup>

<sup>1</sup>Institute of Advanced Energy, Kyoto University, Gokasho, Uji, Kyoto 611-0011, Japan

<sup>2</sup>Institute for Solid State Physics, The University of Tokyo, Kashiwa, Chiba 277-8581, Japan

Layered Mn-based transition metal oxides have gained interest as positive electrode materials for K-ion batteries due to their high capacity, excellent structural stability, and abundant resources. However, their practical utility is significantly hindered by insufficient electrochemical performances during operations. This study reports the successful synthesis of P3-K<sub>0.46</sub>MnO<sub>2</sub> via the solid-state method and investigates its charge–discharge behavior as a positive electrode working in an FSA-based (FSA= bis (fluorosulfonyl)amide) ionic liquid electrolyte at 298 K. The K<sub>0.46</sub>MnO<sub>2</sub> electrode demonstrates superior performance compared to previously reported K<sub>x</sub>MnO<sub>2</sub> counterparts, delivering a reversible discharge capacity of about 100 mAh g<sup>-1</sup> at a current density of 20 mA g<sup>-1</sup> and a capacity retention of 68.3% over 400 cycles at 100 mA g<sup>-1</sup>. Ex situ X-ray diffraction analyses confirm the occurrence of reversible structural changes during the charge–discharge process. Further, we explore potassium storage mechanisms through ex situ synchrotron soft X-ray absorption spectroscopy. Spectra obtained in Mn L-edge region suggest that Mn is reversibly oxidized and reduced during K<sup>+</sup> deintercalation and intercalation processes. Remarkably, discharging the electrode below 2.3 V induces reversible formation of Mn<sup>2+</sup> from Mn<sup>3+/4+</sup> on the electrode surface. The study demonstrates superior electrochemical performance of K<sub>0.46</sub>MnO<sub>2</sub> positive electrode for K-ion battery using ionic liquid electrolyte.

© 2024 The Author(s). Published on behalf of The Electrochemical Society by IOP Publishing Limited. This is an open access article distributed under the terms of the Creative Commons Attribution Non-Commercial No Derivatives 4.0 License (CC BY-NC-ND, <http://creativecommons.org/licenses/by-nc-nd/4.0/>), which permits non-commercial reuse, distribution, and reproduction in any medium, provided the original work is not changed in any way and is properly cited. For permission for commercial reuse, please email: [permissions@iopublishing.org](mailto:permissions@iopublishing.org). [DOI: [10.1149/1945-7111/ad803a](https://doi.org/10.1149/1945-7111/ad803a)]



Manuscript submitted July 24, 2024; revised manuscript received September 9, 2024. Published October 9, 2024.

Supplementary material for this article is available [online](#)

Since their first commercialization in 1991, rechargeable Li-ion batteries (LIBs) have become top-tier energy storage systems that have played a critical role in the deployment of renewable energy resources and accelerated innovations in portable electronics, electric vehicles (EV) and smart grid systems.<sup>1–3</sup> Despite their high energy densities, the advancement of LIBs has been heavily restricted by the uneven geological distribution of lithium (Li) and cobalt (Co) resources and their associated price volatility. Consequently, research interests have shifted to alternative energy materials based on abundant elements such as sodium (Na) and potassium (K), whose weight ratios in the Earth's crust have been ranked sixth (Na, 2.36 wt%) and seventh (K, 2.09 wt%), respectively. The focus on Na and K chemistries is further enhanced by their poor alloy formation with aluminum (Al), which allows the use of Al current collectors as cheaper substitutes for the copper ones used in LIBs.<sup>4</sup> As such, Na-ion batteries (NIBs) and K-ion batteries (KIBs) are uniquely positioned to replace LIBs for future energy storage needs.

On this front, KIBs offer several advantages over NIBs. For instance, the standard redox potential of K<sup>+</sup>/K in most solvents is closer to that of Li<sup>+</sup>/Li and lower than that of Na<sup>+</sup>/Na,<sup>5,6</sup> suggesting that KIBs could achieve operating voltages comparable to LIBs and surpass those of NIBs. Moreover, the inexpensive and commonly used graphite negative electrodes for LIBs have been found to facilitate reversible K<sup>+</sup> intercalation and deintercalation, further promoting KIB viability.<sup>7,8</sup> Notably, K<sup>+</sup> has the smallest Stokes' radius<sup>9</sup> and the lowest desolvation energy in the Li<sup>+</sup>, Na<sup>+</sup> and K<sup>+</sup> line-up,<sup>10</sup> endowing it with the highest diffusivity in electrolytes and the fastest electrode reactions—favorable qualities for practical battery operations.

Despite the benefits highlighted so far, the larger ionic radius of K<sup>+</sup> (1.38 Å), compared to that of Na<sup>+</sup> (1.02 Å) and Li<sup>+</sup> (0.76 Å),<sup>4,9,11</sup> is thought to potentially induce significant structural deterioration of the active material during electrochemical

operations. Drawing inspiration from the success of the LiCoO<sub>2</sub> positive electrode in LIBs,<sup>12,13</sup> layered transition metal oxides with K<sub>x</sub>MO<sub>2</sub> (M = transition metal element, 0 < x ≤ 1) compositions have become promising positive electrode materials for KIBs due to their low cost, nontoxicity and excellent structural stability. The K<sub>x</sub>MO<sub>2</sub> framework comprises two-dimensional slabs formed by edge-sharing MO<sub>6</sub> octahedra. In these structures, K<sup>+</sup> is accommodated between two adjacent MO<sub>2</sub> layers at the octahedral (O3-type) or prismatic (P2- or P3-type) sites. As with other layered oxides, the digits in the O3-, P2-, or P3-type notations represent the unique periodicity of the MO<sub>2</sub> slab stacking.<sup>14</sup> The feasibility of K<sub>x</sub>MO<sub>2</sub> positive electrodes was highlighted by distorted P2-K<sub>0.3</sub>MnO<sub>2</sub> positive electrode reported for KIBs in 2016,<sup>15</sup> which brought the merits of Mn adoption into perspective. Following this milestone, several other K<sub>x</sub>MnO<sub>2</sub>-type positive electrodes, such as P3-K<sub>0.5</sub>MnO<sub>2</sub><sup>16,17</sup> and P3-K<sub>0.45</sub>MnO<sub>2</sub>,<sup>18,19</sup> have been successfully synthesized, inspiring explorations into other elements, such as Fe,<sup>20</sup> Cr,<sup>21,22</sup> and Co.<sup>23</sup> These advancements establish the viability of layered transition metal oxides as positive electrodes and certify K<sub>x</sub>MnO<sub>2</sub> as an attractive platform for KIB development.

The safety of rechargeable batteries has also become an area of concern due to the numerous reports of fire accidents caused by the flammable and volatile organic electrolytes over the years. Consequently, ionic liquid (IL) electrolytes have gained traction as prospective electrolyte candidates for safe battery operations due to their outstanding thermal stabilities, moderate conductivities, and wide electrochemical windows.<sup>24</sup> In fact, considerable research efforts have gone into the development of ionic liquids based on amide anions such as FSA (bis(fluorosulfonyl)amide), TFSA (bis(trifluoromethylsulfonyl)amide) and FTA (fluorosulfonyl(trifluoromethylsulfonyl)amide) to harness their favorable properties for electrolyte applications in batteries. Some ILs, such as 1-allyl-3-vinylimidazolium bis(fluorosulfonyl)amide, contribute to the formation of uniform and stable SEI, which allows the electrode to withstand significant volume changes and maintain structural integrity during the charge and discharge cycles. Furthermore, the IL shows good resistance to Al corrosion.<sup>25</sup> Against this background, a previous study by our research group also pioneered the

\*Electrochemical Society Member.

<sup>2</sup>E-mail: [yamamoto.takayuki.2w@kyoto-u.ac.jp](mailto:yamamoto.takayuki.2w@kyoto-u.ac.jp)

development of an IL electrolyte, K[FSA]–[C<sub>3</sub>C<sub>1</sub>pyrr][FSA] (C<sub>3</sub>C<sub>1</sub>pyrr = *N*-methyl-*N*-propylpyrrolidinium), for KIBs.<sup>26</sup> Figure S1 shows the chemical structure of *N*-methyl-*N*-propylpyrrolidinium cation and bis(fluorosulfonyl)amide anion. Our report further demonstrated that potassium has a more negative redox potential than lithium and sodium in M[FSA]–[C<sub>3</sub>C<sub>1</sub>pyrr][FSA] (M = Li, Na and K) ionic liquids, suggesting the potential development of KIBs with high operating voltages. Subsequent investigations using our IL electrolyte have also shown that a variety of negative electrodes, such as graphite<sup>27,28</sup> and alloy-based materials,<sup>29,30</sup> can deliver reasonable performances in KIBs. By this token, the K[FSA]–[C<sub>3</sub>C<sub>1</sub>pyrr][FSA] IL electrolyte can be expected to facilitate safe and stable KIB operations alongside K<sub>x</sub>MnO<sub>2</sub> positive electrodes.

Although the P3-type manganese oxide K<sub>x</sub>MnO<sub>2</sub> has been studied as positive electrode material for K-ion battery, almost all of them used organic solvent electrolytes and the research on its behavior in ionic liquids is still limited. Therefore, in this study, we evaluate the charge–discharge behavior of P3–K<sub>0.46</sub>MnO<sub>2</sub> positive electrode with the aid of the K[FSA]–[C<sub>3</sub>C<sub>1</sub>pyrr][FSA] IL electrolyte for KIBs. The morphology, elemental distribution and composition, and crystal structure of the K<sub>0.46</sub>MnO<sub>2</sub> powdered active material are characterized through scanning electron microscopy, energy-dispersive X-ray spectroscopy, inductively coupled plasma-atomic emission spectroscopy and ex situ powder X-ray diffraction. Further, we discuss the electrochemical behavior and working mechanism of the K<sub>0.46</sub>MnO<sub>2</sub> positive electrode in the IL electrolyte using insights drawn from galvanostatic charge–discharge tests, ex situ X-ray diffraction, and ex situ synchrotron-based soft X-ray absorption spectroscopy.

## Experimental

**Synthesis of P3–K<sub>0.46</sub>MnO<sub>2</sub>.**—The present K<sub>0.46</sub>MnO<sub>2</sub> was synthesized using Mn<sub>2</sub>O<sub>3</sub> (Sigma-Aldrich, 99.9% purity) and K<sub>2</sub>CO<sub>3</sub> (Sigma-Aldrich, 99.99% purity) via the solid-state method. A mixture of K<sub>2</sub>CO<sub>3</sub> and Mn<sub>2</sub>O<sub>3</sub> with a molar ratio of 0.52:1 was homogeneously mixed and ground in a mortar before being calcined in air. A stoichiometric K<sub>0.46</sub>MnO<sub>2</sub> composition was obtained using K<sub>2</sub>CO<sub>3</sub> in the excess amount of 15 wt% to compensate for the potassium loss during calcination. The calcination temperature was increased at the rate of 5 K min<sup>−1</sup> to 1123 K, and maintained for 15 h. Subsequently, the final sample was naturally cooled to 573 K and transferred into an open dry chamber. After additional grinding in the open dry chamber, the as-synthesized K<sub>0.46</sub>MnO<sub>2</sub> powder was stored in an Ar-filled glove box (H<sub>2</sub>O, O<sub>2</sub> < 0.5 ppm).

**Materials characterizations.**—The elemental composition of the K<sub>0.46</sub>MnO<sub>2</sub> powder was determined through inductively coupled plasma-atomic emission spectroscopy (ICP-AES; Spectroblue, Hitachi). The surface morphology and elemental distribution were detected via scanning electron microscopy (SEM; Phenom Pro Generation 5, Thermo Fisher Scientific) and energy-dispersive X-ray spectroscopy (EDS; SE1200–8001, Thermo Fisher Scientific). Prior to the SEM analysis, the surface of the as-synthesized K<sub>0.46</sub>MnO<sub>2</sub> powder was coated with Au to improve its conductivity. X-ray diffraction patterns of the as-synthesized K<sub>0.46</sub>MnO<sub>2</sub> powder and positive electrodes at different charge–discharge states were obtained by using an X-ray diffractometer (XRD; Ultima IV, Rigaku) with a Cu-K $\alpha$  radiation ( $\lambda$  = 1.5418 Å). Further, ex situ synchrotron-based soft X-ray absorption spectroscopy (sXAS) was employed to detect the electronic states of K<sub>0.46</sub>MnO<sub>2</sub> at their Mn L-edge and O K-edge regions at BL-11 of the SR center (Ritsumeikan University, Japan). The samples were treated in the Ar-filled glove box and transferred to the XRD and sXAS apparatuses with airtight vessels to prevent contact with air.

**Electrochemical measurements.**—The charge–discharge performance of K<sub>0.46</sub>MnO<sub>2</sub> electrode was evaluated using CR2032-type

coin cells assembled in the Ar-filled glove box. Potassium metal (Sigma-Aldrich, 98% purity) and a two-ply glass fiber (Whatman, GF/A, thickness: 260  $\mu$ m) were used as the counter electrode and separator, respectively. The working electrode was fabricated by mixing the K<sub>0.46</sub>MnO<sub>2</sub> active material with acetylene black and poly(tetrafluoroethylene) at the weight ratio of 85:10:5 before pressing the resultant composite film on an Al mesh. The loading mass of active material in each electrode was approximately 8.5 mg cm<sup>−2</sup>. The electrolyte used in the present study was prepared by mixing K[FSA] salt (Nippon Shokubai Co., Ltd., purity  $\geq$ 99%) with [C<sub>3</sub>C<sub>1</sub>pyrr][FSA] ionic liquid (Kanto Chemicals Co., Ltd.) at a composition of  $x$ (K[FSA]) = 0.20 ( $x$ : molar fraction), commensurate with a K[FSA] molar concentration of 0.98 mol L<sup>−1</sup> at 298 K.<sup>26</sup> Galvanostatic charge–discharge tests were performed on the electrodes using a potentiostat (580-type battery cycler, Scribner Associates, Inc.) set in the voltage range of 1.5–4.0 V at 298 K. Furthermore, the corrosiveness of the aluminum mesh current collector in the K[FSA]–[C<sub>3</sub>C<sub>1</sub>pyrr][FSA] IL electrolyte was investigated by a chronoamperometric measurement at a constant voltage of 4.0 V applied to K/Al two-electrode coin cell.

## Results and Discussion

The efficacy of the present preparation method was ascertained through a series of chemical and characterization measurements. Table S1 shows the elemental composition of the as-synthesized powder determined through ICP-AES analysis. The K:Mn atomic ratio was found to be 0.46:1, confirming the successful fabrication of a stoichiometric K<sub>0.46</sub>MnO<sub>2</sub> composition via the solid-state method. XRD measurements were performed with the aid of an airtight holder due to the hygroscopic nature of the synthesized powder. As shown in Fig. 1a, the obtained pattern appears identical to the calculated pattern from P3-type K<sub>0.5</sub>MnO<sub>2</sub> with *R3m* space group.<sup>31</sup> The P3-type structure is schematically illustrated in Fig. 1b. Figure S2 shows the XRD pattern of the as-synthesized K<sub>0.46</sub>MnO<sub>2</sub> powder alongside one obtained from a powder sample exposed to air for comparison. The exposure to air results in a lower shift in the diffraction angle of the main peaks appearing around 13.9° and 27.9° and produces a set of unknown peaks in the 35°–68° range, confirming the instability of K<sub>0.46</sub>MnO<sub>2</sub> in air at room temperature. The SEM images in Fig. 1c reveal the as-synthesized K<sub>0.46</sub>MnO<sub>2</sub> powder consists of 1–2  $\mu$ m sized primary particles that aggregate into 3–6  $\mu$ m sized secondary particles. The effectiveness of the present synthesis method is further confirmed by EDS mappings (Figs. 1d–1f), which display a uniform elemental distribution of O, K and Mn on the as-synthesized K<sub>0.46</sub>MnO<sub>2</sub>. The EDS spectrum in Fig. S3 illustrates characteristic K and Mn peaks that correspond to the weight ratios of 13.3% and 39.9%, respectively. This composition of K and Mn equates to an atomic ratio of K:Mn = 0.47:1, in consistency with the ICP-AES results.

Figures 2a and 2b illustrate the charge–discharge behavior and rate performance of a K<sub>0.46</sub>MnO<sub>2</sub> positive electrode working in the IL electrolyte in the 1.5–4.0 V voltage window at varied current densities. The electrode delivers discharge capacities of 139, 93.3, 76.0, 67.6, 52.6, and 33.1 mAh g<sup>−1</sup> at the current densities of 20, 40, 80, 100, 200, 500 mA g<sup>−1</sup>, respectively. The initial charge and discharge capacities are 67.5 and 139 mAh g<sup>−1</sup>, commensurate with deintercalation of 0.26 K<sup>+</sup> and intercalation of 0.54 K<sup>+</sup>, respectively. The electrochemical behavior of the electrode is characterized by a capacity decay when current densities increase. Nonetheless, the discharge capacity bounces back up to 100 mAh g<sup>−1</sup> when the current density is reset to 20 mA g<sup>−1</sup> from 500 mA g<sup>−1</sup>, indicating the structural deterioration in the K<sub>0.46</sub>MnO<sub>2</sub> electrode is minimal. The cyclability of the K<sub>0.46</sub>MnO<sub>2</sub> electrode was further investigated at 100 mA g<sup>−1</sup> for 400 cycles, as shown in Figs. 2c and S4. The positive electrode yields an initial discharge capacity of 57.7 mAh g<sup>−1</sup> and exhibits a low-capacity decay of approximately 0.05 mAh g<sup>−1</sup> per cycle throughout the cycling process. The discharge capacities retained at the 100th cycle (50.3 mAh g<sup>−1</sup>) and 400th cycle

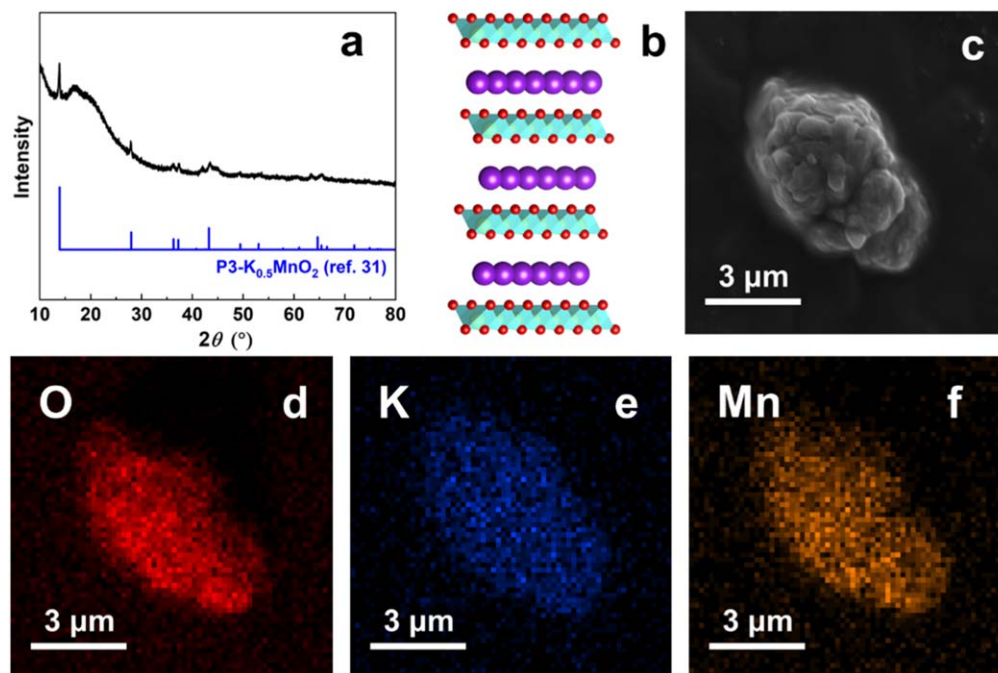


**Figure 1.** Structural characterization of the as-synthesized  $K_{0.46}MnO_2$  powder. (a) XRD pattern (b) schematic diagram of the crystal structure, (c) SEM image, (d)–(f) EDS mapping images of O, K and Mn.

( $39.4 \text{ mAh g}^{-1}$ ) correspond to capacity retentions of 87.2% and 68.3%, respectively. The average coulombic efficiency over the 400 cycles was found to be higher than 99%. Compared to the capacities at  $100 \text{ mA g}^{-1}$  in this cyclability test,  $K_{0.46}MnO_2$  electrode exhibits the higher capacity in the rate capability test (Figs. 2a and 2b), which is possibly caused by the pre-activation during operation at low current densities in early cycles. It is worth noting that the charge–discharge curves virtually retain their shapes even after cycling for 400 cycles (Fig. S4), demonstrating the robust structure of the  $K_{0.46}MnO_2$  positive electrode can stably facilitate continued  $K^+$  intercalation and deintercalation processes. Table I summarizes the electrochemical performance of previously reported  $K_xMnO_2$  ( $0.21 \leq x \leq 0.5$ ) electrodes for comparison with the present electrode.<sup>17–19,32,33</sup> Compared to those  $K_xMnO_2$  electrodes operating in organic solvent electrolytes, the  $K_{0.46}MnO_2$  positive electrode in this study exhibits the superior electrochemical performance, which might be contributed by the formation of stable CEI<sup>25</sup> and the suppression of Mn dissolution<sup>34</sup> in the IL electrolyte. However, we think the  $K_{0.46}MnO_2$  is still subjected to slight decomposition of the electrolyte on electrode surface and the

Jahn-Teller effect of  $Mn^{3+}$ <sup>18,19,31</sup> during charge and discharge processes, which leads to the slight capacity decrease with cycling. Furthermore, as shown in Fig. S5, the corrosive behavior of the aluminum mesh current collector in the  $K[FSA]-[C_3C_1pyrr][FSA]$  IL electrolyte was investigated by applying a constant voltage of 4.0 V to the K/Al two-electrode coin cell. The current density was calculated with the geometric surface area of aluminum mesh current collector ( $0.785 \text{ cm}^2$ ). The anodic current density decreases to  $1.87 \mu\text{A cm}^{-2}$  within 1 min and it is stabilized at a low value of  $0.175 \mu\text{A cm}^{-2}$  after 72 h, indicating the  $K[FSA]-[C_3C_1pyrr][FSA]$  IL electrolyte also exhibits an excellent tolerance against the Al corrosion.

As shown in Fig. 3, the crystal structural changes occurring in the  $K_{0.46}MnO_2$  positive electrode were examined through ex situ XRD analyses performed on electrodes at different charge and discharge states of the first cycle operated at  $20 \text{ mA g}^{-1}$  in 1.5–4.0 V. The main peak of  $K_{0.46}MnO_2$  at around  $13.9^\circ$  is assigned to the 003 diffraction. Upon charging to 3.9 V, a peak shift of the 003 diffraction toward lower angle is observed, which corresponds to increased interlayer spacing (along with  $c$  axis) possibly due to the

**Table I. Summary of the electrochemical performance of the present  $K_{0.46}MnO_2$  positive electrode and representative  $K_xMnO_2$  electrodes from previous studies.**

Electrolyte	Active materials	Initial discharge capacity (mAh g <sup>-1</sup> ) @ current density (mA g <sup>-1</sup> )	Working voltage range (V)	Capacity retention @ <i>n</i> th cycle/current density (mA g <sup>-1</sup> )	References
1 M K[FSA] in [C <sub>3</sub> C <sub>1</sub> pyrr][FSA]	P3- $K_{0.46}MnO_2$	139 @ 20	1.5–4.0	50.3 @ 100/100	This study
				39.4 @ 400/100	
0.7 M KPF <sub>6</sub> in EC: DEC (1:1 in vol.)	P3- $K_{0.5}MnO_2$	106 @ 5	1.5–3.9	81 @ 20/5	17
		140 @ 5		47 @ 20/5	
0.8 M KPF <sub>6</sub> in EC: DEC (1:1 in vol.)	P3- $K_{0.45}MnO_2$	121 @ 20	1.5–4.0	59.7 @ 100/20	18
	P3- $K_{0.45}MnO_2$	116.3 @ 20	1.5–4.0	60.4 @ 100/20	19
	P2- $K_{0.21}MnO_2$	98.1 @ 20	1.5–3.9	49.5 @ 100/20	33
1 M KPF <sub>6</sub> in EC: DEC: PC (1:1:1 in vol.)	P3- $K_{0.23}MnO_2$	87.7 @ 20	1.5–3.9	44.8 @ 100/20	32
	$K_{0.32}MnO_2$	95.1 @ 10	2.0–4.5	36.1 @ 100/100	

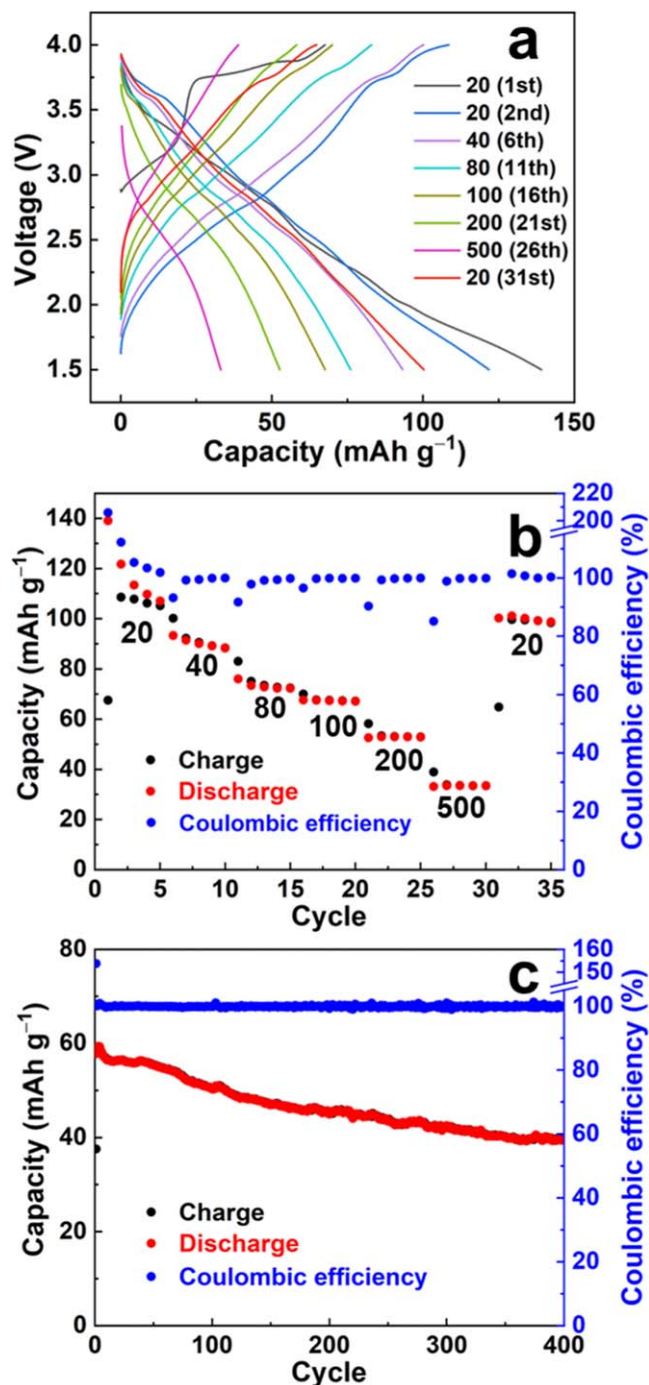


**Figure 2.** (a), (b) Charge–discharge curves and rate performance of the  $K_{0.46}MnO_2$  positive electrode at the current rates of 20, 40, 80, 100, 200, 500  $mA g^{-1}$ . (c) Capacity retention and coulombic efficiency over 400 cycles performed at a current rate of 100  $mA g^{-1}$  in the 1.5–4.0 V voltage range.

increase of the oxygen–oxygen Coulombic repulsion induced by the deintercalation of  $K^+$  from the structure.<sup>17,35</sup> In addition, the emergence of unknown peaks around  $10.8^\circ$ ,  $21.9^\circ$  and  $36.3^\circ$  is confirmed. When the cell is charged to 4.0 V, these unknown peaks remain and the 003 diffraction peak disappears. During the discharge process, the 003 diffraction peak appears again at 3.3 V, and a set of the unknown peaks disappears at 3.0 V. Then, upon discharging from 3.0 V to 1.5 V, the 003 diffraction peak shifts to higher angle, which corresponds to the decrease of interlayer spacing caused by lowering the Coulombic repulsion during the intercalation of  $K^+$

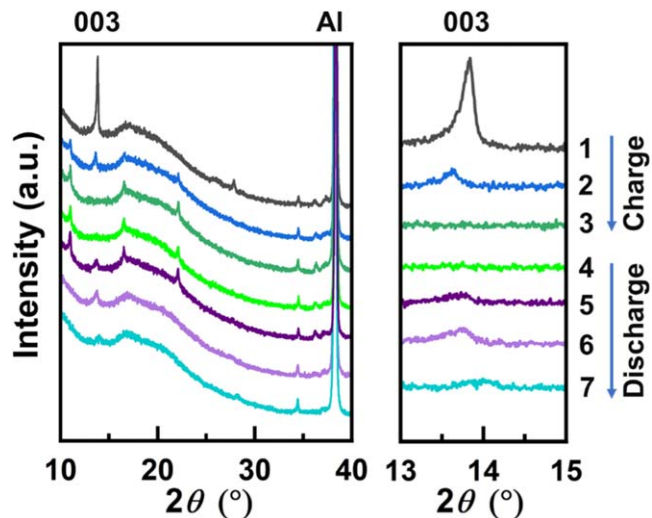


**Figure 3.** XRD patterns and magnifications of  $K_{0.46}MnO_2$  positive electrodes at different charge–discharge states during the 1st cycle conducted at a current rate of 20  $mA g^{-1}$  in the 1.5–4.0 V voltage range. (1) Pristine, (2) charge to 3.9 V, (3) charge to 4.0 V, (4) discharge to 3.9 V, (5) discharge to 3.3 V, (6) discharge to 3 V, and (7) discharge to 1.5 V.

ions. The reversible formation of the unknown peaks is a marked difference to previous research<sup>16–19,31</sup> on the crystal evolutions of  $K_xMnO_2$  positive electrode during cycling. A possible reason for this phenomenon is the reversible migration of Mn into K layer accompanied by a phase transition. The migration of transition metal elements has been confirmed for many layered transition metal oxide materials in Li- and Na-ion batteries, such as irreversible migration of Mn in O3- $Li_{0.5}MnO_2$ <sup>36</sup> and reversible migration of Fe in P2- $Na_{0.67}Mn_{0.66}Fe_{0.20}Cu_{0.14}O_2$ .<sup>37</sup> It seems that the reversible migration is easier to occur in the transition metal oxides with P-type structure than those with O-type structure.<sup>37</sup> In any case, the diffraction pattern at the fully discharged state is remarkably resemblant to the one from the pristine electrode, highlighting the structural stability of the  $K_{0.46}MnO_2$  positive electrode during the charge–discharge process.

For insights into the mechanisms of  $K^+$  intercalation and deintercalation into/from the  $K_{0.46}MnO_2$  positive electrode, ex situ sXAS measurements were performed on the electrodes under the total electron yield (TEY; detection depth: 10 nm) and partial fluorescence yield (PFY; detection depth: 100 nm)<sup>38</sup> modes. Figures 4 and S6 show the electronic states of Mn L-edge and O K-edge during the 1st charge–discharge cycle conducted in the 1.5–4.0 V voltage range at a current rate of 20  $mA g^{-1}$ , respectively. The Mn L-edge and O K-edge spectra of MnO ( $Mn^{2+}$ ),  $Mn_2O_3$  ( $Mn^{3+}$ ) and  $MnO_2$  ( $Mn^{4+}$ ) were also obtained for reference purposes. The spectra obtained in Mn L-edge region under the TEY mode (Fig. 4a) show the pristine  $K_{0.46}MnO_2$  electrode comprises a  $Mn^{3+}$  signal around 640 eV and a  $Mn^{4+}$  signal around 642 eV. During charging to 4.0 V, the  $Mn^{3+}$  peak becomes weaker, while a slightly higher energy peak shift is observed at around 652 eV (see the enlarged view in Fig. S7). This observation is ascribed to the oxidation of  $Mn^{3+}$  to  $Mn^{4+}$  during the  $K^+$  deintercalation process. The Mn L-edge spectra obtained during the discharge (reduction) process appear to form a trace in the opposite direction of the charge process, further affirming the reversibility of the process. When the electrode was discharged to 3.0 V, the intensity ratio between the 640 eV peak and the 642 eV peak becomes larger than the one observed at the charging end, suggesting that a fraction of the  $Mn^{4+}$  in the active material was reduced to  $Mn^{3+}$  during the discharge process. On an interesting note, a  $Mn^{2+}$  signal is detected around 638 eV in the TEY mode spectrum (Fig. 4a) when the electrode is further discharged to 2.3 V. The Mn L-edge spectra taken in the TEY mode in the subsequent

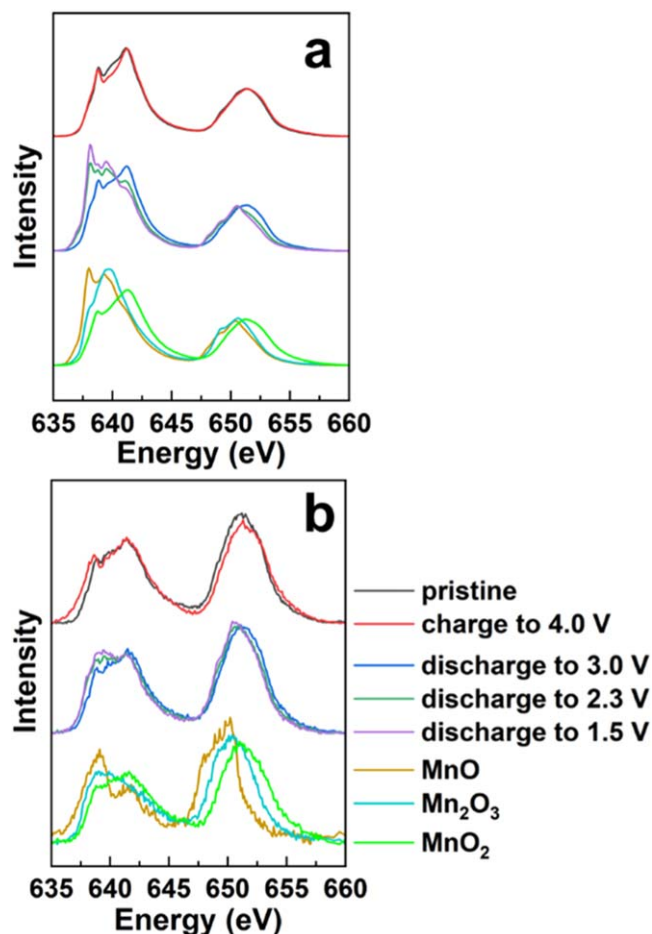


**Figure 4.** Ex situ Mn L-edge sXAS spectra of the  $K_{0.46}\text{MnO}_2$  positive electrode during the 1st charge–discharge cycle conducted at a current rate of  $20 \text{ mA g}^{-1}$  in the 1.5–4.0 V voltage range under the (a) total electron yield (TEY) and (b) partial fluorescence yield (PFY) modes.

charge–discharge cycles (up to 10 cycles) are provided in Fig. S8a. The spectrum obtained under the TEY mode during the 2nd cycle shows the peak intensity of the  $\text{Mn}^{2+}$  decreases when the electrode is charged to 2.7 V. The spectra from the subsequent cycles revert to the trend observed in the 1st cycle, maintaining it up to the 10th cycle under both the TEY (Fig. S8a) and PFY modes (Fig. S8b). This behavior suggests that the Mn reaction during charge–discharge processes is reversible and additionally confirms the cycling stability of the  $K_{0.46}\text{MnO}_2$  electrode. A Mn L-edge sXAS spectrum was also taken in the TEY mode after the  $K_{0.46}\text{MnO}_2$  electrode was discharged to 1.5 V directly from its pristine state, as shown in Fig. S9. The obtained spectrum appears to be identical to the electrode discharged to 1.5 V during the 1st cycle. In contrast, the  $\text{Mn}^{2+}$  peaks in the spectra taken in the PFY mode (Figs. 4b and S8b) are barely detectable even after discharging to 1.5 V: an indication that the  $\text{Mn}^{2+}$  formation is limited to the surface region of active material. The O K-edge spectra in Figs. S6a and S6b indicate that the  $K_{0.46}\text{MnO}_2$  electrode consists of a pre-edge region (below 532 eV) and a broad band region (above 532 eV). The pre-edge region is attributed to the hybridization of Mn 3d and O 2p orbitals, while the broad band region is ascribed to the hybridization of the Mn 4sp and O 2p orbitals.<sup>39</sup> Given that the pre-edge peak is influenced by variations in the hole states of the hybridized Mn 3d–O 2p orbital, its intensity is expected to increase when  $\text{Mn}^{2+}$  oxidizes to  $\text{Mn}^{4+}$ . Accordingly, the intensity of the O K-edge pre-edge peaks is seen to increase during charge and decrease during discharge, suggesting that  $\text{K}^+$  deintercalation process was accompanied by the oxidation from  $\text{Mn}^{3+}$  to  $\text{Mn}^{4+}$  whereas the  $\text{K}^+$  intercalation involves the

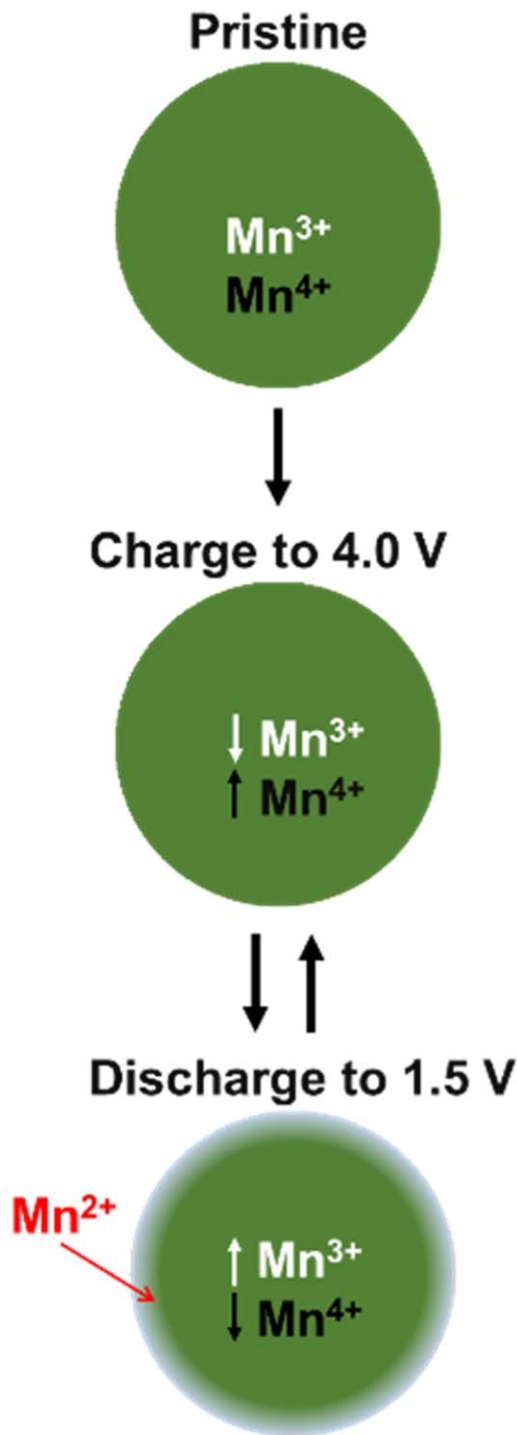


**Figure 5.** Schematic illustration of charge–discharge mechanisms of the  $K_{0.46}\text{MnO}_2$  positive electrode during operations in the voltage range of 1.5–4.0 V.

reduction from  $\text{Mn}^{4+}$  to  $\text{Mn}^{3+}$  and eventually to  $\text{Mn}^{2+}$ . The trends observed in the O K-edge spectra are in good alignment with those from the Mn L-edge spectra, further validating the charge–discharge mechanisms discussed in this study.

Figure 5 shows the schematic illustration of the charge–discharge mechanisms occurring in the  $K_{0.46}\text{MnO}_2$  positive electrode during operations in the 1.5–4.0 V voltage range. When the electrode is charged to 4.0 V, a fraction of the  $\text{Mn}^{3+}$  in the  $K_{0.46}\text{MnO}_2$  is oxidized to  $\text{Mn}^{4+}$ . On the other hand, the discharge process is characterized by a reversion of the Mn valence to its original state at

3.0 V. A further drop of voltage to below 2.3 V is seen to prompt the formation of  $\text{Mn}^{2+}$  on the surface of the  $\text{K}_{0.46}\text{MnO}_2$  positive electrode.

### Conclusions

In summary, layered  $\text{P3-K}_{0.46}\text{MnO}_2$ , synthesized via the solid-state method, was employed as a positive electrode material for a K-ion battery using a  $\text{K}[\text{FSA}]-[\text{C}_3\text{C}_1\text{pyrr}][\text{FSA}]$  ionic liquid electrolyte. The structure of the  $\text{K}_{0.46}\text{MnO}_2$  electrode was demonstrated to facilitate a stable reversible  $\text{K}^+$  intercalation and deintercalation processes over 400 cycles. Further, compared to previously reported  $\text{K}_x\text{MnO}_2$  positive electrodes, the electrode in this study delivered a superior electrochemical performance (discharge capacity: 100 mAh  $\text{g}^{-1}$  at the current rate of 20 mA  $\text{g}^{-1}$ ; 68.3% capacity retention after 400 cycles at 100 mA  $\text{g}^{-1}$ ). XRD and sXAS analyses determined that the Mn in the  $\text{K}_{0.46}\text{MnO}_2$  electrode underwent reversible redox reactions involving  $\text{Mn}^{3+}$  to  $\text{Mn}^{4+}$  during the charge–discharge cycles above 3.0 V. However, reversible formation of  $\text{Mn}^{2+}$  (from the  $\text{Mn}^{3+}$ ) was found to occur on the electrode surface when the electrode was discharged to below 2.3 V. The results presented in this study prove  $\text{K}_{0.46}\text{MnO}_2$  to be a positive electrode material with superior electrochemical performance and structural stability for KIB using an FSA-based ionic liquid electrolyte.

### Acknowledgments

This study was partially supported by the Iwatani Naoji Foundation, ISHIZUE 2023 of Kyoto University and JSPS KAKENHI grant (JP24K01602). We would like to thank Nippon Shokubai Co., Ltd. for supplying the  $\text{K}[\text{FSA}]$  salt. K. Jiao would also like to thank the Ministry of Education, Culture, Sports, Science, and Technology of Japan (MEXT) for scholarship support. The authors declare no competing financial interest.

### ORCID

Takayuki Yamamoto  <https://orcid.org/0000-0003-3553-3272>  
Toshiyuki Nohira  <https://orcid.org/0000-0002-4053-554X>

### References

1. M. Armand and J. M. Tarascon, *Nature*, **451**, 652 (2008).
2. Z. P. Cano, D. Banham, S. Ye, A. Hintennach, J. Lu, M. Fowler, and Z. Chen, *Nat. Energy*, **3**, 279 (2018).
3. B. Dunn, H. Kamath, and J. Tarascon, *Science*, **334**, 928 (2011).
4. T. Hosaka, K. Kubota, A. S. Hameed, and S. Komaba, *Chem. Rev.*, **120**, 6358 (2020).
5. S. G. Bratsch, *J. Phys. Chem. Ref. Data*, **18**, 1 (1989).
6. Y. Marcus, *Pure Appl. Chem.*, **57**, 1129 (1985).
7. Z. Jian, W. Luo, and X. Ji, *J. Am. Chem. Soc.*, **137**, 11566 (2015).
8. S. Komaba, T. Hasegawa, M. Dahbi, and K. Kubota, *Electrochem. Commun.*, **60**, 172 (2015).
9. R. D. Shannon, *Acta Crystallogr., Sect. A*, **32**, 751 (1976).
10. M. Okoshi, Y. Yamada, S. Komaba, A. Yamada, and H. Nakai, *J. Electrochem. Soc.*, **164**, A54 (2017).
11. Y. Matsuda, *J. Electrochem. Soc.*, **128**, 2552 (1981).
12. K. Mizushima, P. C. Jones, P. J. Wiseman, and J. B. Goodenough, *Mater. Res. Bull.*, **15**, 783 (1980).
13. A. Yoshino, *Angew. Chem. Int. Ed.*, **51**, 5798 (2012).
14. X. Zhang, Z. Wei, K. N. Dinh, N. Chen, G. Chen, F. Du, and Q. Yan, *Small*, **16**, 2002700 (2020).
15. C. Vaalma, G. A. Giffin, D. Buchholz, and S. Passerini, *J. Electrochem. Soc.*, **163**, A1295 (2016).
16. B. Peng, Y. Li, J. Gao, F. Zhang, J. Li, and G. Zhang, *J. Power Sources*, **437**, 226913 (2019).
17. H. Kim, D. Seo, J. C. Kim, S. Bo, L. Liu, T. Shi, and G. Ceder, *Adv. Mater.*, **29**, 1702480 (2017).
18. C. Liu, S. Luo, H. Huang, X. Liu, Y. Zhai, and Z. Wang, *Chem. Eng. J.*, **378**, 122167 (2019).
19. C. Liu, S. Luo, H. Huang, Y. Zhai, and Z. Wang, *ChemElectroChem*, **6**, 2308 (2019).
20. K. Jiao, T. Yamamoto, H. Kiuchi, H. Zhao, and T. Nohira, *J. Electrochem. Soc.*, **171**, 040529 (2024).
21. N. Naveen, S. C. Han, S. P. Singh, D. Ahn, K. Sohn, and M. Pyo, *J. Power Sources*, **430**, 137 (2019).
22. H. Kim, D. Seo, A. Urban, J. Lee, D. Kwon, S. Bo, T. Shi, J. K. Papp, B. D. McCloskey, and G. Ceder, *Chem. Mater.*, **30**, 6532 (2018).
23. Y. Hironaka, K. Kubota, and S. Komaba, *Chem. Commun.*, **53**, 3693 (2017).
24. T. Yamamoto and T. Nohira, *Chem. Rec.*, **23**, e202300169 (2023).
25. M. Gu, A. M. Rao, J. Zhou, and B. Lu, *Energy Environ. Sci.*, **16**, 1166 (2023).
26. T. Yamamoto, K. Matsumoto, R. Hagiwara, and T. Nohira, *J. Phys. Chem. C*, **121**, 18450 (2017).
27. H. Onuma et al., *ACS Energy Lett.*, **5**, 2849 (2020).
28. T. Yamamoto, A. Yadav, and T. Nohira, *J. Electrochem. Soc.*, **169**, 050507 (2022).
29. T. Yamamoto and T. Nohira, *Chem. Commun.*, **56**, 2538 (2020).
30. Y. Domi, H. Usui, K. Kuritani, N. Wada, K. Nishikawa, T. Yamamoto, T. Nohira, and H. Sakaguchi, *ACS Appl. Energy Mater.*, **6**, 11583 (2023).
31. M. K. Cho, J. H. Jo, J. U. Choi, and S.-T. Myung, *ACS Appl. Mater. Interfaces*, **11**, 27770 (2019).
32. S. Chong, Y. Wu, Y. Chen, S. Guo, Z. Tai, C. Shu, Q. Tan, J. Sun, and Y. Liu, *Electrochim. Acta*, **293**, 299 (2019).
33. T. Liu, S. Hou, Y. Li, S. Xue, J. Hu, H. Fu, C. Yang, and L. Zhao, *J. Energy Chem.*, **64**, 335 (2022).
34. C. G. Torres-Castaneda, G. Evmenenko, N. S. Luu, P. M. Das, W. J. Hyun, K.-Y. Park, V. P. Dravid, M. C. Hersam, and M. J. Bedzyk, *ACS Appl. Mater. Interfaces*, **15**, 35664 (2023).
35. L. Wu, H. Fu, W. Lyu, L. Cha, A. M. Rao, K. Guo, J. Zhou, S. Wen, and B. Lu, *ACS Nano*, **18**, 13415 (2024).
36. S. Choi and A. Manthiram, *J. Electrochem. Soc.*, **149**, A1157 (2002).
37. E. Talaie, S. Y. Kim, N. Chen, and L. F. Nazar, *Chem. Mater.*, **29**, 6684 (2017).
38. Q. Shen, Y. Liu, L. Jiao, X. Qu, and J. Chen, *Energy Storage Mater.*, **35**, 400 (2021).
39. W. S. Yoon, M. Balasubramanian, K. Y. Chung, X. Q. Yang, J. Mcbreen, C. P. Grey, and D. A. Ficher, *J. Am. Chem. Soc.*, **127**, 17479 (2005).